Experimental Study of Dynamic Icing Process on a Pitot Probe Model

Haiyang Hu,* Faisal Al-Masri,† Linchuan Tian,* and Hui Hu‡
Iowa State University, Ames, Iowa 50011-2271

https://doi.org/10.2514/1.T6782

An experimental study was conducted to characterize the dynamic ice accretion process over the surface of a typical aeronautic Pitot probe model under different icing conditions. The experimental study was conducted in the Icing Research Tunnel available at Iowa State University. While a high-speed imaging system was used to record the dynamic ice accretion process, a three-dimensional (3D) scanning system was also used to measure the 3D shapes of the ice layers accreted on the test model. While opaque and grainy ice structures were found to accrete mainly along the wedge-shaped lip of the front port and over the front surface of the probe holder under a dry rime icing condition, much more complicated ice structures with transparent and glazy appearance were observed to cover almost entire surface of the Pitot probe under a wet glaze icing condition. While a flower-like ice structure was found to grow rapidly along the front port lip, multiple irregular-shaped ice structures accreted over the probe holder under a mixed icing condition. The characteristics of the icing process under different icing conditions were compared in terms of 3D shapes of the ice structures, the profiles of the accreted ice layers, the ice blockage to the front port, and the total ice mass on the Pitot probe model. The acquired ice accretion images were correlated with the 3D ice shape measurements to elucidate the underlying icing physics.

I. Introduction

AIRCRAFT icing is widely recognized as one of the most severe hazards to aircraft operating in cold weathers [1–4]. Ice accumulation over airframe surfaces of an airplane has been found to degrade its aerodynamic performance significantly by increasing aerodynamic drag while decreasing lift [5], causing the airplane to stall at much higher speeds and lower angles of attack than normal under a moderate or severe icing condition [6]. Ice was reported to accumulate on every exposed frontal surface of an airplane, not only on the wings, propellers, and windshields but also on antennas, vents, intakes, cowlings, and Pitot probes mounted on the airplane [6,7].

A Pitot probe, also known as Pitot tube, is a crucial component used to measure the flight speed of an airplane. A Pitot probe is usually composed of a slender tube with distinct holes. While the front hole is faced to the incoming airstream to measure the total pressure of the airstream (i.e., stagnation pressure), the side holes measure the static pressure of the airstream. The airspeed (i.e., airplane flight speed) can be determined based on the difference between the measured total and static pressures, i.e., the dynamic pressure of the airstream [8,9]. Pitot probes are usually mounted on an airplane in various ways, including jutting out from the edge of the wing or sticking up from the fuselage. When an airplane flies through clouds under frozen cold conditions, Pitot probes are very susceptible to the direct impingement of airborne supercooled water droplets in the clouds with the consequence of ice formation/accretion. Ice accretion on Pitot probes can partially or completely block the holes for air pressure measurements, leading to false readings of the measured airspeed. The misreading of the airspeed from iced Pitot probes may directly threaten the aircraft inflight safety, leading to the loss of control over the aircraft [10]. The importance of proper icing control/protection for Pitot probes is highlighted by the deadly aircraft crashes in recent years, including the catastrophic crash of Saratov Airlines Flight 703, which killed all 65 passengers and 6 crew members on February 2, 2018 [11].

Although extensive studies were conducted to investigate aircraft icing physics and to develop effective anti-/de-icing strategies for aircraft icing mitigation, most of the previous studies focused on the icing process over airfoil/wing surfaces. While Pitot probe icing phenomena have been found to be problematic as early as 1938 [12], only limited investigations can be found in the literature to study the fundamental icing physics and anti-/de-icing of Pitot probes. Ozcer et al. [13] conducted a numerical study to examine the ice accretion characteristics over the surface of a Pitot tube under various icing conditions. Zhang et al. [14] reported a numerical investigation to characterize Pitot probe icing phenomena, and found that ambient temperature would have the most significant effects on the icing-induced failure time for Pitot probes. De Souza et al. [15] conducted theoretical and experimental studies to examine the conjugated heat transfer process associated with the transient thermal characteristics of heated aeronautical Pitot probes. Jäckel et al. [16] conducted an experimental study to characterize the effects of inner composition and material properties on the icing process over a Pitot probe. Performance runs were carried out in order to analyze the thermal response of the Pitot probe under various operating conditions with an emphasis on the cooling process for the scenario with a heating element failure. The failure time of the electrical heating system for the Pitot probe icing protection was examined and predicted. A number of icing detection systems designed for Pitot probe icing protection were also explored in recent years to increase the reliability of aeronautics Pitot probe systems [17–19].

Advancing the technology for safer and more efficient aircraft operations in atmospheric icing conditions requires the development of effective and robust anti-/de-icing strategies tailored specifically for Pitot probe icing protection. Doing so requires a keen understanding of the underlying physics pertinent to Pitot probe icing phenomena. While important findings about the ice accretion on Pitot probes were revealed from the previous studies, many of them were based on numerical simulations with simplified assumptions. For the limited experimental studies available in the literature, the majority of the measurement data were relevant to the evaluation of the overall performance of the electrical heating systems used for Pitot probe icing protection. Many important microphysical processes (i.e., unsteady heat transfer, transient surface water runback, and dynamic ice accretion process) pertinent to Pitot probe icing phenomena are still not clearly understood. More comprehensive experimental investigations are desirable to gain further insight into

Presented as Paper 2022-1913 at the AIAA SciTech 2022 Forum, San Diego, CA, January 3–7, 2022; received 13 November 2022; revision received 31 December 2022; accepted for publication 2 January 2023; published online 25 January 2023.

*Postdoctoral, Department of Aerospace Engineering.
†Graduate Student, Department of Aerospace Engineering.
‡Martin C. Jischke Professor, Department of Aerospace Engineering; huhui@iastate.edu. Associate Fellow AIAA (Corresponding Author).

the underlying icing physics as well as to establish a comprehensive experimental database for the validation and verification of the theoretical models and numerical simulations of Pitot probe icing process. Such quantitative experimental databases are also essential for the development of more effective and robust anti-/de-icing strategies for better Pitot probe icing protection.

In the present study, a comprehensive experimental campaign was conducted to quantify the characteristics of dynamic ice accretion process over the surface of a typical Pitot probe under different icing conditions. The icing experiments were performed by leveraging the unique Icing Research Tunnel available at Iowa State University (i.e., ISU-IRT) with a typical aeronautic Pitot probe model exposed to typical dry rime, wet glaze, and mixed icing conditions. During the experiments, while a high-speed imaging system was used to record the dynamic icing process on the surface of the Pitot probe model, three-dimensional (3D) shapes of the ice layers accreted on the test model were also measured quantitatively by a 3D profiler scanning system based on a novel digital image projection (DIP) technique. The acquired ice accretion images were correlated with the 3D shape measurements of the iced Pitot probe model to elucidate the underlying icing physics. The quantitative measurement results obtained from the present study can be further utilized for the validation and verification of the theoretic modeling and numerical simulations of the Pitot probe icing process under different icing conditions.

II. Experimental Setup and Test Model

A. Icing Research Tunnel Used for the Present Study

The experimental study was performed in the ISU-IRT, which is a newly refurbished, multifunctional icing research tunnel. As shown schematically in Fig. 1, the ISU-IRT has a test section with four optically transparent sidewalls. The test section is 2.0 m in length, 0.4 m in width, and 0.4 m in height. It has a capacity of generating a maximum wind speed of 65 m/s with the temperature down to −25°C. An array of nine spray nozzles/atomizers (IKEUCHI BIMV 8002) was mounted inside the ISU-IRT to inject micro-sized water droplets into the airflow. Based on the measurement results of the LaVision's ParticleMaster™ system, the water droplets in the ISU-IRT were found to range from 10 to 100 μm in size with the mean volume diameter of about 20 μm. By manipulating the pressure and flow rate supplied to the atomizer/spray nozzles, the liquid water content (LWC) levels of the airflow in the ISU-IRT can be adjusted in the range from 0.1 to 5.0 g/m^3. In summary, the ISU-IRT can be used to simulate atmospheric icing phenomena over a wide range of icing conditions, i.e., from very dry rime to extremely wet glaze ice conditions representative of typical aircraft icing envelopes. Further information about the ISU-IRT and its usage for various atmospheric icing and anti-icing studies is available in our recent publications [20–23].

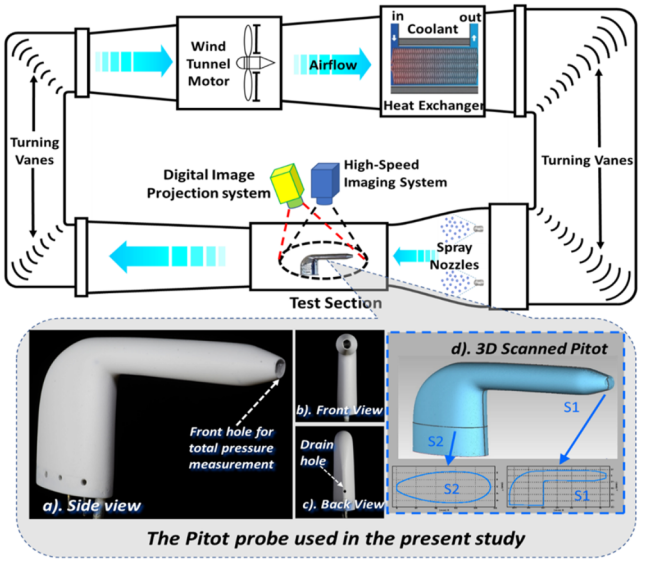

Fig. 1 Schematic of the experimental setup and the test model used in the present study.

B. Pitot Probe Model Used in the Present Study

In the present study, a simple, commercially available aeronautic Pitot probe (i.e., model PH 502 series made by Aero Instrument Co.) was used as the test model for the icing experiments. As shown in Fig. 1, the test model is "L" shaped (135 mm in length and 55 mm in width). It consists of a total pressure tube (i.e., stagnation port) and an airfoil-shaped probe holder. The total pressure tube is cylindrical in shape with an outer diameter of 16 mm (i.e., $D_{\text{outer}} = 16.0$ mm) and 88 mm in tube length. The Pitot probe has a wedge-shaped front port with a hole inner diameter of 6.0 mm for the total pressure measurement. The Pitot probe holder, which is used to mount the Pitot probe onto the airframe surface, has a symmetric airfoil shape with the airfoil chord length ranging from 38 to 54 mm. A draining hole was designed to locate at the trailing edge of the probe holder to drain out the collected moisture/water during the operation [11].

The surface of the Pitot probe used for the present study was wet sanded by using fine sandpapers (i.e., up to 2000 grit) to achieve a smooth, glossy finish with a characteristic surface roughness of about 20 μm. A thin layer of all-weather-protective spray-on enamel coating (Rustoleum™, Flat Protective Enamel) was also applied to the surface of the Pitot probe model. It should be noted that the wettability of the enamel-coated mode surface was found to be very similar to that of the original nickel-coated surface. The static contact angle (CA) of the enamel-coated surface was found to be $CA_{\text{static}} \approx 60°$, while $CA_{\text{static}} \approx 58°$ for the original nickel-coated probe surface. During the experiments, the Pitot probe model was mounted horizontally in the middle of the ISU-IRT test section with the angle of attack (AOA) of zero in relation to the incoming airflow (i.e., AOA = 0°).

C. Controlling Parameters Used for the Icing Experiments

It is well known that ice accretion over an airframe surface can be categorized as *rime*, *glaze*, or *mixed icing*, depending on the ambient conditions under which the icing event occurs [24–28]. When the ambient temperature is relatively low (i.e., typically below −8.0°C) and the airflow is relatively dry (i.e., having a lower LWC), supercooled water droplets carried by the incoming airflow would freeze immediately after impacting onto the airframe surface, forming rime ice. At relatively warmer temperatures, i.e., just below the water freezing temperature (i.e., typically above −8.0°C), with a relatively high LWC level for the incoming airflow, the impinged supercooled water droplets would be frozen only partially, with the remaining impacted water mass running back along the ice accreting surface. The runback water would be frozen into ice subsequently at further downstream locations, forming glaze ice with much more complex ice shapes. *Mixed icing* refers to the situation with a simultaneous appearance of both rime and glaze icing characteristics.

In the present study, while the speed of the incoming airflow in the ISU-IRT was kept constant (i.e., $V_\infty = 40$ m/s) during the icing experiments, the characteristics of the rime, glaze, and mixed icing processes on the Pitot probe were investigated by changing the ambient temperature and LWC levels of the incoming airflow. More specifically, while the operation parameters of the ISU-IRT were set to $V_\infty = 40$ m/s, $T_\infty = -15$°C, and $LWC = 0.50$ g/m^3 for the typical rime icing experiment, the corresponding values become $V_\infty = 40$ m/s, $T_\infty = -5$°C, and $LWC = 2.0$ g/m^3 for the typical glaze icing experiment. The characteristics of the mixed icing processes were studied under the test conditions of $V_\infty = 40$ m/s and $T_\infty = -5$°C, while the LWC levels of the incoming airflow were changed from $LWC = 0.50$ to 2.0 g/m^3. In summary, the corresponding Reynolds number based on the outer diameter of the total pressure tube (i.e., $D_{\text{outer}} = 16$ mm) is estimated to be $Re \approx 50,000$ for all the test cases of the present study.

Following up on the work of Anderson [29] and Waldman and Hu [20], a nondimensional parameter called *ice accumulation parameter* is usually used to characterize the ice accretion process over an airframe surface. The ice accumulation parameter A_c used in the present study is defined as

$$A_c = \frac{LWC \cdot V_\infty \cdot t}{\rho_{\text{ice}} \cdot l} \tag{1}$$

where LWC refers to the liquid water content of the incoming airflow; V_∞ is the incoming airflow velocity; t is the ice accretion time; ρ_{ice} is the density of the accreted ice; and l is the characteristic length of the test model (i.e., the outer diameter of the Pitot probe model for the present study). As given in Eq. (1), for the same incoming airflow velocity and the same Pitot probe model used in the present study, the value of the ice accumulation parameter of A_C would vary linearly with the LWC value and the ice accretion time t. To ensure a fair comparison of the test results under different icing conditions, the ice accumulation parameter of A_C can be considered as the nondimensionalized ice accretion time with the effects of the LWC value being corrected.

D. Measurement Systems Used for the Icing Experiments

During the experiments, two sets of high-speed imaging systems (PCO Tech, Dimax™ with acquisition rate up to 25,000 frames per second at the spatial resolution of 2048 pixels by 2048 pixels) along with 60 mm Macro-lenses (Nikon, 60 mm Nikkor 2.8D) were used to acquire the dynamic ice accretion process over the surface of the Pitot probe from two different perspective views (i.e., one is used to provide the side view, and the other providing the bottom view). A pair of 150 W fiber-coupled halogen lamps (AmScope, HL250-AS) were used to provide low-flicker illumination to ensure the good quality of the acquired ice accretion images. The two digital cameras were connected to a workstation (i.e., host computer) via a digital delay generator (Berkeley Nucleonics, Model 565) to control the timing of the image acquisition. With the experimental setup used in the present study, the spatial resolution of the acquired ice accretion images was found to be about 15 pixels/mm.

In addition to using the high-resolution cameras to record the dynamic ice accretion process, a novel DIP-based 3D profile scanning system [30–32] was also used to quantify the 3D shapes of the iced Pitot probe model under different icing conditions. The DIP system is based on the principle of structured light triangulation in a fashion similar to the stereo vision technique but replacing one of the cameras in the stereo pair with a digital projector [32]. A digital image with known pattern characteristics was projected onto the test object of interest (i.e., ice structures accreted over the model surface for the present study). Due to the complex 3D geometrical profiles of the test objects (i.e., the surface of the accreted ice structures), the projected digital patterns would be deformed when observed from a perspective different from the projection axis. By comparing the distorted digital patterns (i.e., acquired images with ice structures accreted over the surface of the test model) with a reference digital pattern without the test objects on the reference surface, the 3D profile of the iced test model can be retrieved quantitatively. Further information about the technical basis and implementation of the DIP system is available in Gao et al. [30] and Zhang et al. [32].

After conducting a careful calibration operation to register the quantitative relationship between the digital projector and high-resolution camera, the iced Pitot probe model was rotated every 30 deg around its center for the DIP image acquisitions. The DIP images were processed to retrieve 3D profiles of the ice structures acquired at different phase angles, and then combined automatically to reconstruct the 3D shapes of the ice structures accreted on the test model. For the measurement results given in the present study, the field of view for the 3D scanning system was set to be 200 mm by 200 mm. During the 3D scanning operation, while the airflow in the ISU-IRT was paused, the ambient temperature was kept at the same level as the ice accretion experiment. While it usually takes about 60 s to scan the 3D shapes of the ice layers accreted over the surface of the test model for each case, the change in the morphology of the accreted ice structures is believed to be very small due to the scanning operation. Based on the results of a calibration procedure similar to that reported by Veerakumar et al. [33], the measurement accuracy of the 3D profile scanning system was found to be about 0.20 mm in measuring the 3D shapes of the ice layers accreted over the test model.

While a typical 3D scanning result of the Pitot probe before conducting the ice accretion experiment was given in Fig. 1d, the two-dimensional (2D) profiles of the test model at two typical planes (i.e., S_1 is along the midplane of the probe's front port, and S_2 is in a typical cross section of the probe holder) were extracted from the 3D scanning result. Similar to those shown in Fig. 1d, the quantitative measurement data, such as the outer profiles of the ice layers accreted on the model surface at any cross sections, and the total volume (thereby, the total mass of the ice structures accreted on the Pitot probe model), can be obtained based on the 3D scanning results, which will be presented and discussed in the following section of the present study.

It should be noted that the research work presented here is a fundamental icing physics study with the primary objective to elucidate the underlying physics for a better understanding of Pitot probe icing phenomena. While the test model used in the present study is a simple Pitot probe, the icing experiments were conducted with a much lower incoming airflow speed in comparison to the flight speed of the realistic aircraft. The effects of the design/operation parameters of the Pitot probes used for a specific aircraft on the ice accretion process are beyond the scope of the present study. A comprehensive experimental study to examine the effects of important design/operation parameters of Pitot probes (e.g., probe geometry, materials of the probes, and the working Mach numbers) on the dynamic ice accretion over the surface of Pitot probes is planned, and the research findings will be reported in the future.

It should also be noted that an electrical heating element was embedded inside the probe holder for the Pitot probe model used in the present study. However, because the primary objective of the present study is to quantify the characteristics of the dynamic ice accretion process over the surface of the Pitot probe under different icing conditions, the electrical heating element was switched off all the time during the icing experiments. A follow-up investigation will also be conducted to explore and evaluate the effectiveness of the electrical heating for the Pitot probe icing mitigation and protection.

III. Experimental Results and Discussion

A. High-Speed Imaging Results to Visualize the Dynamic Icing Process over the Surface of the Pitot Probe Model Under Typical Rime and Glaze Icing Conditions

Before starting the icing experiments, the ISU-IRT was operated at the prescribed frozen-cold temperatures (e.g., $T_\infty = -5.0°C$ for the glaze and mixed icing experiment, and $T_\infty = -15.0°C$ for the rime icing experiments) for at least 30 minutes without switching on the water spray system to ensure that the ISU-IRT reached a thermal steady state. After turning on the water spray system of the ISU-IRT, micro-sized water droplets in the ISU-IRT would be cooled down rapidly to become airborne, super-cooled water droplets. The supercooled water droplets carried by the frozen-cold airflow would impinge onto the surface of the Pitot probe model to start the icing process. Two high-resolution imaging systems were synchronized with the switch of the water spray system to capture the time sequences of the ice accretion images to reveal the dynamic icing process over the model surface from two different perspectives.

Figure 2 shows the time sequences of the acquired snapshot images to reveal the dynamic ice accretion process over the surface of the Pitot probe under the typical dry rime icing condition of $V_\infty = 40$ m/s, $T_\infty = -15°C$, and $LWC = 0.5$ g/m^3. As described by Liu and Hu [21], under such as dry and cold test condition, the heat transfer process (i.e., both convective and conductive heat transfer) over the surface of the Pitot probe model would be conducted very intensively to remove/dissipate all the latent heat of fusion released during the phase-changing (i.e., solidification) process of the impinged supercooled water droplets instantly. Therefore, the water droplets were frozen into solid ice immediately upon impacting onto the Pitot probe model. As a result, ice accretion would take place only at the locations where the airborne supercooled water droplets impinged upon. As revealed clearly in Fig. 2, corresponding to the unique "L" shape of the Pitot probe model used in the present study, ice accretion on the test model was found to take place primarily at

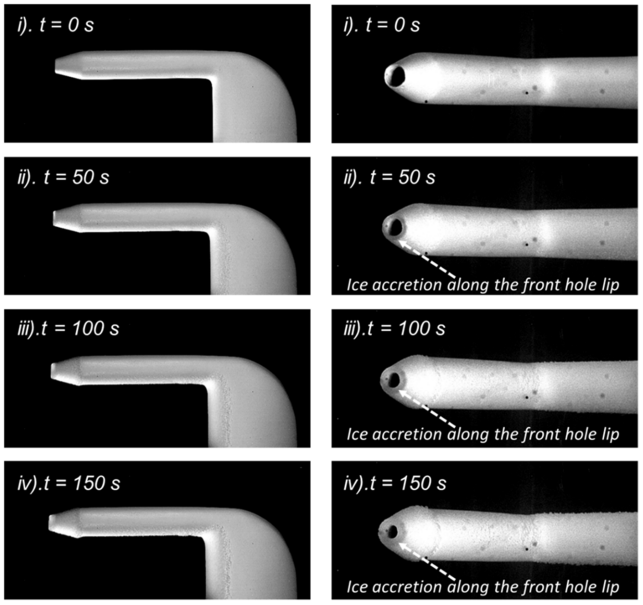

a) Side view b) Bottom view

Fig. 2 Typical snapshot images to reveal the dynamic ice accretion process on the Pitot probe under the rime icing condition of $V = 40$ m/s, $T_\infty = -15.0°C$, and $LWC = 0.50$ g/m^3.

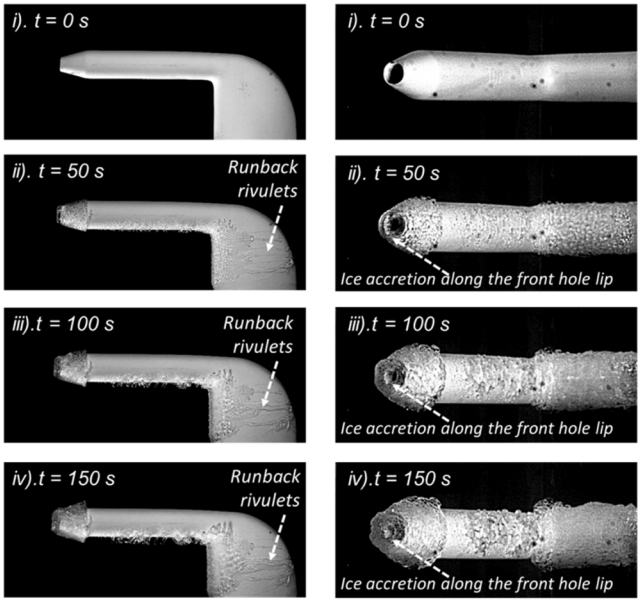

a) Side view b) Bottom view

Fig. 3 Typical snapshot images to reveal the dynamic ice accretion process on the Pitot probe under the glaze icing condition of $V_\infty = 40$ m/s, $T_\infty = -5.0°C$, and $LWC = 2.0$ g/m^3.

two places: 1) over the wedge-shaped front port of the Pitot tube model (i.e., around the lips of the total pressure port), and 2) over the front surface of the airfoil-shaped probe holder. Because the supercooled water droplets were found to be frozen into ice instantly upon impacting onto the probe surfaces, no traces of unfrozen water runback or runback ice accretion were observed on the back surface of the Pitot probe model (i.e., in the regions beyond the direct impinging zone of the airborne water droplets).

It can also be seen clearly that the ice structures accreted over the model surface were opaque and had a milky-white appearance, which exhibits typical rime ice characteristics as described by Hansman and Kirby [28]. While the accreted ice layer over the Pitot probe surface was observed to conform well with the outer profile of the probe model in general, the front surface of the probe model was found to become much rougher and was covered with grainy ice structures due to the entrainment of air bubbles between the rime ice grains [21]. As time increases, with more and more supercooled water droplets impinging onto the model surface, the thickness of the ice layers accreted over on the frontal surfaces of the probe model was found to increase rapidly, especially along the lip of the wedged front port for the total pressure measurement. As a result, the lip of the front port was found to become thicker and thicker, causing a smaller and smaller hole diameter of the front port. The front hole used for the total pressure measurement would be plugged completely due to the ice accretion as the ice accretion time becomes long enough, which would lead to a misreading of the airspeed from the iced Pitot probe.

Figure 3 gives some typical snapshot images to visualize the dynamic ice accreting process on the surface of the same Pitot probe model under the test condition of $V_\infty = 40$ m/s, $T_\infty = -5.0°C$, and $LWC = 2.0$ g/m^3. In comparison to the rime icing case shown in Fig. 2, while the airflow speed was kept at the same level of $V_\infty = 40$ m/s, the LWC level was increased to $LWC = 2.0$ g/m^3 (i.e., four times greater than the rime icing case). Therefore, much more airborne supercooled water droplets would impact onto the Pitot probe model within the same duration of the icing experiment, resulting in a much greater amount of the latent heat of fusion to be released over the surface of the test model. However, both the convective and conductive heat transfer processes over the ice accreting surface became much milder due to the warmer ambient temperature for this test case (i.e., $T_\infty = -5.0°C$). The inadequate heat transfer under such a wetter and warmer icing condition was not able to dissipate all the released latent heat of fusion rapidly, causing the delay in the solidification (i.e., icing) of the impacted supercooled water droplets on the probe surface. As a result, only a portion of the water droplets were found to be frozen into ice upon impacting onto the model surface, and the rest of the impacted water stayed in the liquid phase over the probe surface until all the released latent heat of fusion was dissipated completely.

Driven by the aerodynamic shear force exerted by the incoming airflow, the unfrozen water collected over the front probe surface was found to run back along the ice-accreting surface swiftly, resulting in the formation of multiple rivulets to transport the impacted water from the frontal surface of the probe model to downstream locations (i.e., reaching to the downstream regions beyond the direct impinging zone of the supercooled water droplets). As shown clearly in Fig. 3, the runback rivulet flows were found to extend further downstream as the time increases, eventually reaching the trailing edge of the probe model where the drain hole was located. Because the incoming airflow was set at the frozen temperature of $T_\infty = -5.0°C$ during the icing experiment, the unfrozen water was cooled down continuously as running back and was found to be frozen into ice eventually at further downstream locations. As a result, the even drain hole located at the backside of the Pitot probe model was found to be blocked by the formation of the runback ice structures.

In summary, as revealed clearly in Fig. 3, the ice structures accreted on the probe surface were found to exhibit typical features of the glaze icing process, i.e., forming transparent, glassy ice structures with obvious traces of water runback [28]. The thickness of the ice layer accreted over the front port of the Pitot probe model was found to increase continuously with the increasing ice accretion time. Due to much higher LWC level of the incoming airflow, the ice layer accreted along the lip of the front port of the probe model was found to increase much faster for the glaze icing case, in comparison to the rime icing scenario shown in Fig. 2. As a result, the front hole of the Pitot probe model was found to be more readily plugged (i.e., at a shorter ice accretion time) due to the faster ice accretion under the glaze icing condition.

B. Three-Dimensional Scanning Results to Quantify the Characteristics of the Ice Structures Accreted on the Pitot Probe Model Under Rime and Glaze Icing Conditions

In addition to using high-speed imaging systems to qualitatively visualize the dynamic ice accretion processes, a DIP-based 3D profile scanning system was also used to quantify the 3D shapes of the ice layers accreted on the test model. Figure 4 gives typical 3D scanning

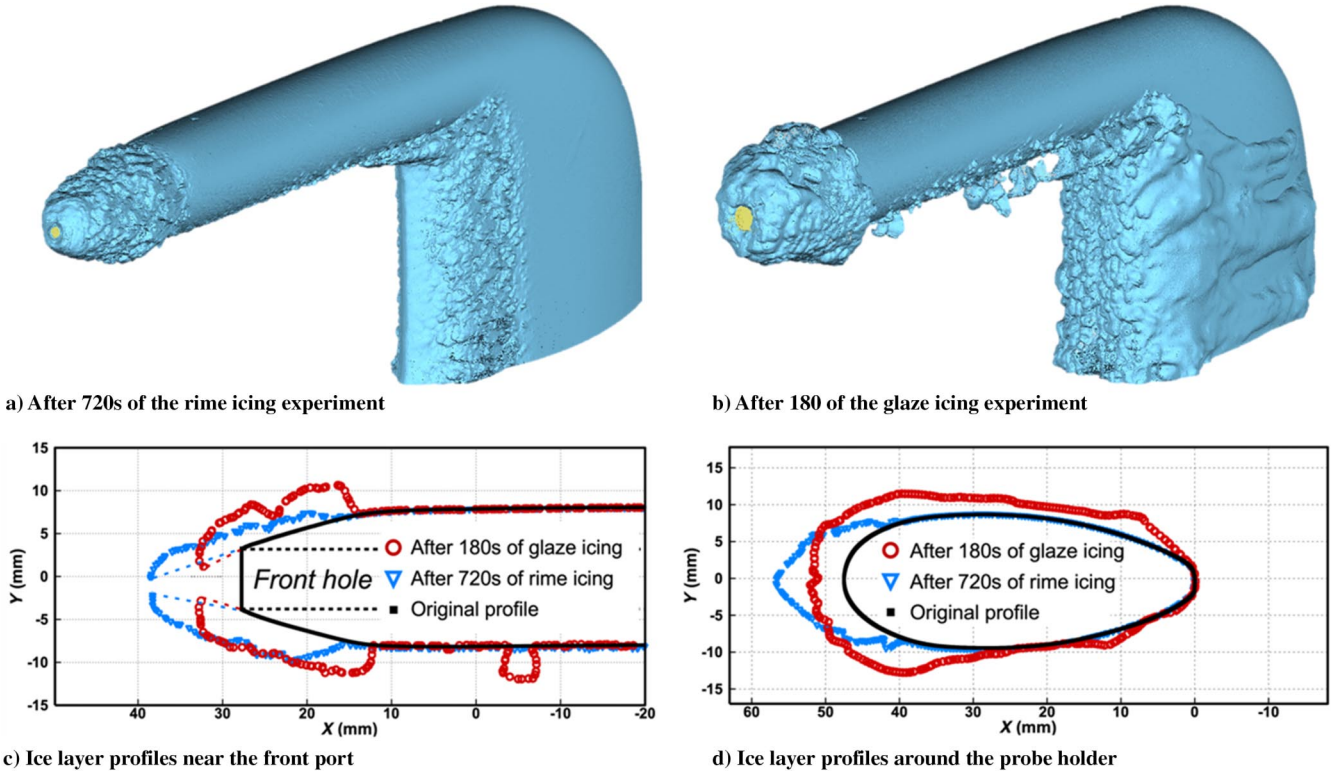

Fig. 4 Three-dimensional scanning results of the ice layers accreted on the Pitot probe model after the rime and glaze icing experiments.

results of the iced Pitot probe model under the glaze and rime icing conditions. Based on the 3D scanning results, the outer profiles of ice layers accreted on the probe model in any cross-sectional planes can be extracted. Typical outer profiles of the ice layers accreted over the probe surface, which were in the symmetrical plane near the front port of the Pitot probe model and in the middle plane of the probe holder (i.e., the S_1 and S_2 planes shown in Fig. 1), were also shown in Fig. 4 to reveal the different characteristics of the rime and glaze icing processes more clearly and quantitatively.

To ensure a fair comparison of the ice accretion characteristics under different icing conditions, the ice accumulation parameter of A_C was kept at the same value for the compared test cases. Based on the definition of the ice accumulation parameter given in Eq. (1), because the incoming airflow velocity was kept as a constant in the present study, the value of the ice accumulation parameter of A_C would vary linearly with LWC value and the ice accretion time t. For the 3D scanning results given in Fig. 4, the ice accumulation parameter of A_C was set to be $A_C \approx 1.0$. Because the LWC level for the rime icing case (i.e., $LWC = 0.50$ g/m^3) is only one-fourth of that of the glaze icing case (i.e., $LWC = 2.0$ g/m^3), the duration of the rime icing experiments (i.e., with a duration of 720 s) was set to be 4.0 times of that of the glaze icing case (i.e., with a duration of 180 s). With such experimental settings, the probe model would be exposed to almost the same amount of airborne supercooled water droplets during the icing experiments under different test conditions.

As revealed quantitatively in Fig. 4a, the accreted ice layers were found to be confined within the direct impinging zones of the supercooled water droplets (i.e., along the lip of the front port for the total pressure measurement and the front surface of the probe holder) after performing 720 s of the rime icing experiment without any traces of water runback on the back surface of the iced probe model. The 3D scanning results also confirmed that the front surface of the iced Pitot probe became much rougher due to the formation of the grainy rime ice structures, and the accreted ice layers conformed well to the original shape of the probe model in general.

It was also revealed clearly in Fig. 4b that, after 180 s of the glaze icing experiment, the ice structures accreted over the surface of the same Pitot probe model were found to become significantly different from those under the rime icing condition. Due to the existence of unfrozen water flow over the model surface under the glaze icing condition, the ice layers accreted over the probe surface were found to have a much wider coverage (i.e., extending to much further downstream locations beyond the direct imping zone of the airborne water droplets). The extracted ice layer profile given in Fig. 4c also reveals that, after the impingements of almost the same amount of airborne supercooled water droplets onto the probe surface, the ice layers accreted along the leading edges of the front port and the probe holder were found to be thinner under the glaze icing condition, in comparison to those under the rime icing condition. Meanwhile, the accreted ice structures on the probe surface were also found to have much more complicated shapes under the glaze icing condition, i.e., forming irregular-shaped ice humps and horn structures, which extruded further into the incoming airflow to catch more airborne supercooled water droplets to accelerate the growth of the glaze ice structures accreted over the probe surface.

Based on the quantitative 3D scanning results given in Fig. 4, the total volumes of the ice layers accreted over the probe surface can also be determined quantitatively, i.e., by subtracting the volumes of the "clean" probe model (i.e., without any ice accretion) from the measured total volumes of the iced probe model. As reported by Liu et al. [25], while the density of typical glaze ice is usually about 900 kg/m^3, the density of rime ice is slightly less, i.e., about 880 kg/m^3, due to the entrainment of air bubbles between rime ice grains. Therefore, the total mass of the ice accreted on the probe model can also be estimated. After being exposed to almost the same amount of the airborne supercooled water droplets, while the measured ice mass accreted on the probe model was found to be about 11.0 g after 180 s of the glaze icing experiment, the corresponding value was only about 6.0 g after 720 s of the rime icing experiment. The significant difference in the measured ice mass accreted on the probe model is believed to be closely related to the different characteristics of the ice accretion process under the rime and glaze icing conditions. In comparison to those accreted under the rime icing condition, more complicated ice structures (i.e., ice humps and horns) were found to accrete over the frontal probe surface under the glaze icing condition, as revealed clearly and quantitatively in Fig. 4. With the Pitot probe model being exposed to almost the same amount of

supercooled water droplets carried by the incoming airflow, the irregular-shaped ice structures (i.e., ice humps and horns) accreted under the glaze icing condition could protrude further into the incoming airflow to catch more airborne water droplets corresponding to the larger projected area of the iced probe model, causing a faster growth of the ice layers accreted over the probe surface. Therefore, 83% more ice mass was found to accrete on the probe surface under the glaze icing condition, in comparison to that of the rime icing case.

C. Effects of the *LWC* Levels of the Incoming Airflow on the Dynamic Ice Accreting Process over the Surface of the Pitot Probe Model

In the present study, a parametric study was also conducted to examine the effects of the LWC levels of the incoming airflow on the dynamic icing process over the surface of the Pitot probe model. During the experiment, with the incoming airflow velocity being $V_\infty = 40$ m/s, the LWC level of the incoming airflow was changed from $LWC = 0.50$ g/m^3 to $LWC = 2.0$ g/m^3, with the ambient temperature being at either $T_\infty = -15$°C or $T_\infty = -5.0$°C. As described above, the ice accumulation parameter of A_C was maintained at the same value of $A_C \approx 1.0$ for all the compared test cases to ensure that the Pitot probe would be exposed to the impingement of almost the same amount of the airborne supercooled water droplets during the icing experiments.

Figure 5 gives the acquired snapshot mages to reveal the dynamic ice accretion processes over the surface of the Pitot probe model for the test cases with relatively cold air temperature of $T_\infty = -15$°C and the LWC level being changed from $LWC = 0.50$ g/m^3 to $LWC = 2.0$ g/m^3. Because the heat transfer process (i.e., both the heat convection via the frozen cold airflow and the heat conduction through the metal substrate) over the ice accreting surface of the test model would be very intensive at the sufficient cold ambient temperature of $T_\infty = -15$°C [21], all the released latent heat of fusion associated with the solidification of the impinged supercooled water droplets was found to be dissipated rapidly for all the test cases (i.e., within the LWC range up to 2.0 g/m^3). As a result, all the supercooled water droplets were found to be frozen into solid ice instantly upon impacting onto the probe surface. As revealed clearly in Fig. 5, while the ice accretion was found to be confined within narrow regions on the front surface of the test model (i.e., within the direct impingement zones of the airborne water droplets near the front lip of the probe and the leading edge of the probe holder), the accumulated ice layers were observed to follow the shape of the Pitot probe model in general. While the accreted ice layers were found to be opaque with milky-white appearance, no obvious water runback was observed on the back surface of the probe model for all the test cases. It suggests that the ice accretion processes had typical rime icing characteristics for all the test cases with the ambient temperature being cold enough (i.e., $T_\infty = -15$°C).

However, as shown clearly in Fig. 6, for the test cases at warmer ambient temperature of $T_\infty = -5.0$°C, the characteristics of the ice accretion processes over the surface of the Pitot probe model were found to vary significantly, depending highly on the LWC level of the test case. This is closely related to the dynamic balance between two competing microphysical processes associated with the ice accretion process [21]: 1) the continuous releasing of the latent heat of fusion associated with the solidification of the impacted supercooled water droplets over the probe surface, and 2) the unsteady heat transfer process to dissipate the released latent heat of fusion from the ice accreting surface. In comparison to the test cases shown in Fig. 5 with much colder ambient temperature (i.e., $T_\infty = -15.0$°C), the heat transfer process (i.e., both convective and conductive heat transfer) would become much weaker due to the warmer ambient temperature (i.e., $T_\infty = -5.0$°C) for the test cases given in Fig. 6, resulting in a much less efficient and slower dissipation of the released latent heat of fusion from the ice accreting surface of the Pitot probe model.

For the test case shown in Fig. 6a, as the LWC level of the incoming airflow was quite low (i.e., $LWC = 0.50$ g/m^3), the total amount of supercooled water droplets impinged onto the Pitot probe surface within a fixed time duration would be limited under such a dry test condition. Therefore, only a very limited amount of the latent heat of fusion would be released within the given time duration associated with the solidification (i.e., icing) of the limited impacted water mass on the model surface. Even though the convective and conductive heat transfer became much weaker, the limited amount of the released latent heat of fusion was still found to be dissipated swiftly under such a dry test condition. As a result, almost all the impacted supercooled water droplets were found to be frozen into ice immediately with no obvious traces of water runback over the surface of the iced Pitot probe model. While ice accretion was found to take place within narrow regions on the front surface of the test model (i.e., near the lip of the front port and near the leading edge of the probe holder), the accreted ice layers were found to be almost opaque with grainy textures, i.e., having very similar characteristics as the typical rime ice structures.

For the test case given in Fig. 6b with the LWC level being increased to $LWC = 1.0$ g/m^3, more supercooled water droplets would impinge onto the surface of the probe model within the same duration of the icing experiment. The total amount of the released latent heat of fusion within the given time duration would increase substantially due to the solidification (i.e., icing) of the greater amount of the collected water mass over the probe surface for this test case. However, because the limited capacity of the convective and conductive heat transfer would not be able to dissipate/remove all the released latent heat of fusion rapidly, a portion of the impacted

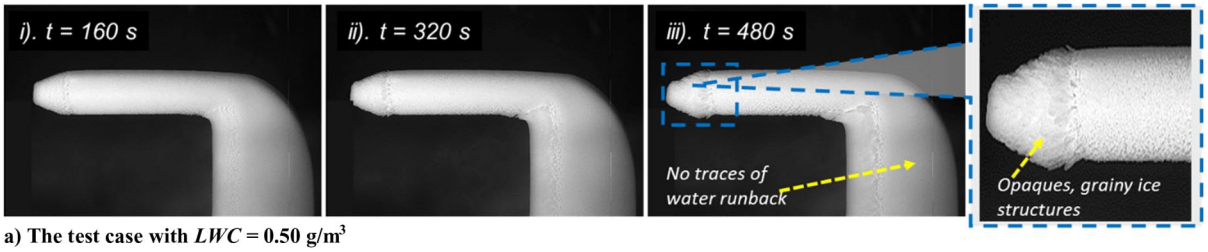

a) The test case with $LWC = 0.50$ g/m^3

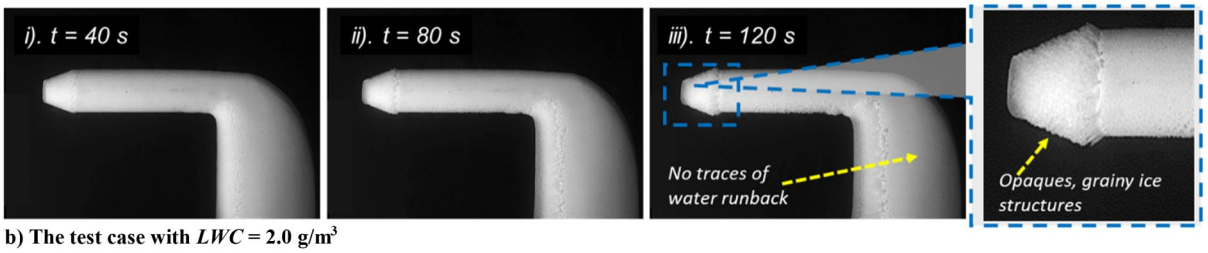

b) The test case with $LWC = 2.0$ g/m^3

Fig. 5 Acquired snapshot images to reveal the dynamic ice accretion processes over the surface of the Pitot probe model with relatively cold ambient temperature of $T_\infty = -15$°C.

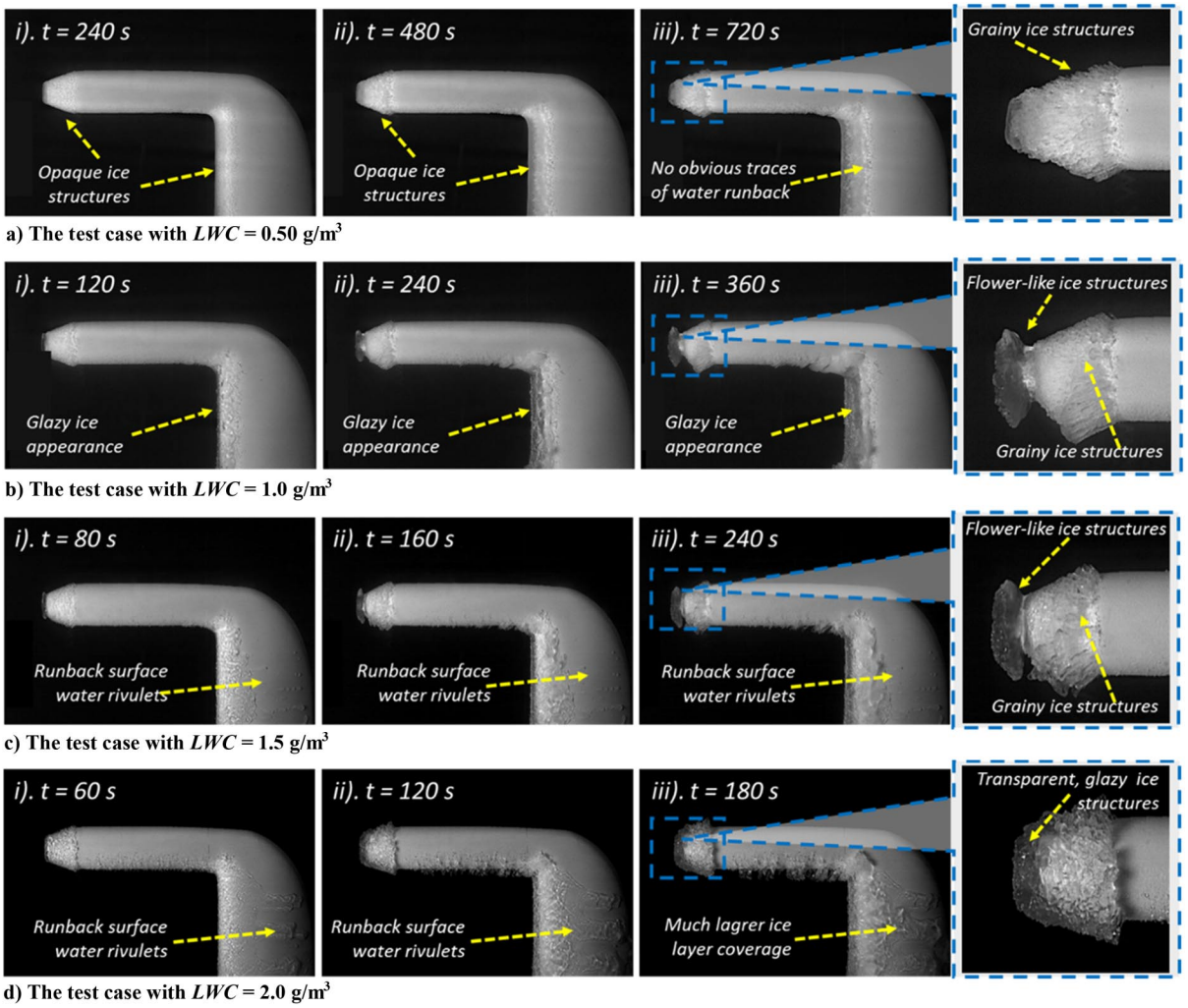

Fig. 6 Acquired snapshot images to reveal the dynamic ice accretion processes over the Pitot probe surface with relatively warmer ambient temperature of $T_\infty = -5°C$.

supercooled water mass droplets would not be able to be frozen into ice instantly, resulting in the existence of unfrozen water on the probe surface. As a result, while some of the ice structures accreted on the probe surface were still found to have grainy-like textures (i.e., a typical feature of rime ice), the existence of the unfrozen water over the ice accreting surface caused the accreted ice layers to become semitransparent or transparent with obvious glazy appearance (i.e., a typical feature for glaze ice). It suggests that the ice accretion under the test condition of $V_\infty = 40$ m/s, $T_\infty = -5°C$, and $LWC = 1.0$ g/m^3 would be a mixed icing process with the appearance of both rime icing and glaze icing characteristics.

It can also be seen that, as driven by the aerodynamic forces exerted by the incoming airflow, the unfrozen water droplets on the ice accreting surface of the probe's front port were pushed to move away from their original sites of impingement. As a result, a distinct, flower-like ice structure was found to grow up along the lip of the front port of the Pitot probe model. The formation of the flower-like ice structure at the probe's front port would enable the accreted ice structures extruding further into the incoming airflow to catch additional airborne water droplets. Therefore, the flower-like ice structure was found to grow up very rapidly as the ice accretion time increases.

As shown clearly in Fig. 6c, as the LWC level of the incoming airflow was further increased to $LWC = 1.50$ g/m^3, much more supercooled water droplets would impact onto the surface of the probe model within the same duration of the icing experiment. It resulted in a significantly greater amount of the latent heat of fusion released over the ice accreting surface of the Pitot probe model. However, due to the limited capacity of the convective and conductive heat transfer to dissipate the released latent heat of fusion from the ice accreting surface at $T_\infty = -5°C$, while only a small portion of the impacted supercooled water droplets were frozen into ice immediately, a significant portion of the impacted water mass would stay in liquid phase until all the released latent heat of fusion was dissipated completely. Driven by the aerodynamic shear forces exerted by the incoming airflow, the unfrozen water accumulated over the front surface of the probe holder was found to run back to form multiple rivulets to transport the unfrozen water mass from the front surface of the test model to much downstream locations (i.e., flowing to downstream locations far beyond the direct impinging zones of the airborne water droplets). While the flower-like ice structure growing from the lip of the probe front port was found to become almost transparent with a lazy appearance (i.e., being more like typical glaze ice structures), the ice layer accreted downstream of the flower-like structure was still found to be in grainy textures (i.e., a typical feature of rime ice). It suggests that, while the ice structures accreted on the probe surface were observed to have a combination of the rime and glaze icing characteristics simultaneously (i.e., being a mixed icing process), the features of glaze ice accretion were found to become much more obvious for this test case, in comparison to those shown in Fig. 6b.

For the test case given in Fig. 6d, because the LWC level was further increased to $LWC = 2.0$ g/m^3, much more supercooled water droplets would be collected over the surface of the Pitot probe model. Due to the insufficient heat transfer to rapidly dissipate the released latent heat of fusion from the ice-accreting surface of the test model, a significant amount of unfrozen water mass was found to accumulate over the front surface of the probe model. Driven by the incoming airflow, the unfrozen water was found to run back from the

front surface of the probe model to much downstream locations swiftly. Because the impacted water was transported away from the front surface rapidly before being frozen into ice for this test case, no obvious flower-like ice structure was observed to grow from the front port of the Pitot probe model. However, because the ambient temperature was still set to be frozen cold at $T_\infty = -5.0°C$, the runback water was found to be cooled down continuously and frozen into ice eventually at further downstream locations. Unlike those forming opaque, grainy rime ice structures under the rime and mixed icing conditions described above, the ice structures accreted over the surface of the probe model for this test case were found to become completely transparent with a distinct glazy appearance, indicating a typical glaze icing process [20]. It can also be seen that, in comparison to those of rime icing and mixed icing scenarios described above, the accreted glaze ice structures were found to have a much wider coverage over the probe surface, and even the drain hole located at the backside of the probe model was blocked due to the formation of the runback ice for the test case.

Figure 7 gives the measurement results of the 3D profile scanning system to quantify the 3D shapes of the iced Pitot probe model as a function of the LWC level of the incoming airflow, with the ambient temperature being kept at $T_\infty = -5.0°C$. Based on the 3D scanning results given in Fig. 7, the extracted profiles of the ice layers accreted on the Pitot probe model in two selected planes (i.e., in the S_1 and S_2 planes, as shown in Fig. 1) are given in Fig. 8 for a direct comparison of the ice accretion characteristics under different icing conditions. As illustrated clearly in Fig. 7a, with the LWC of the incoming airflow being relatively low (i.e., $LWC = 0.5$ g/m^3), the ice structures accreted over the surface of the Pitot probe model were found to concentrate within the narrow regions on the front surface of the probe model with a dominant grainy feature, as expected. The profiles of the accreted ice layers accreted over the Pitot probe surface

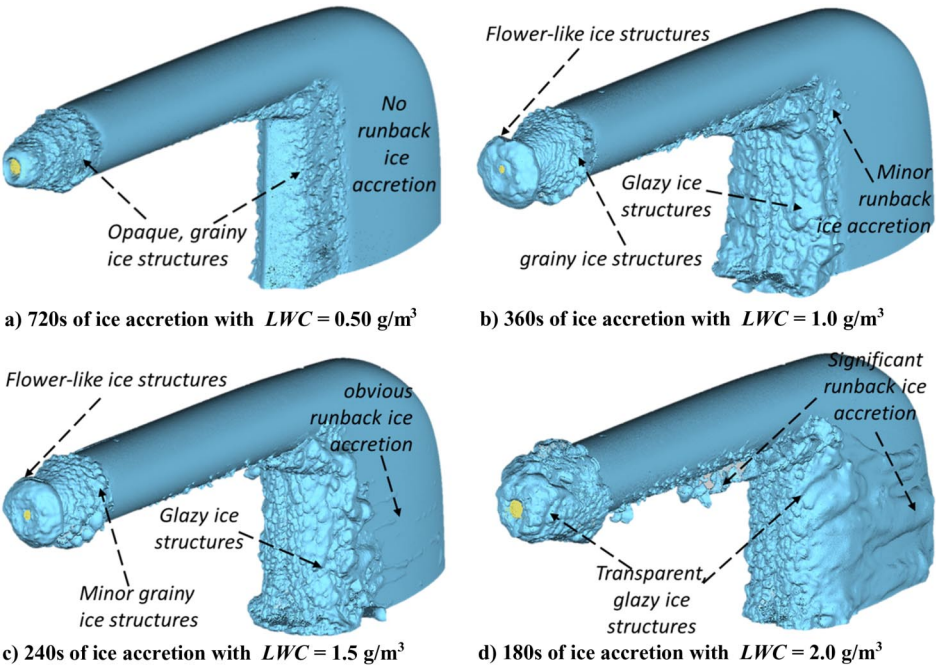

a) 720s of ice accretion with $LWC = 0.50$ g/m^3

b) 360s of ice accretion with $LWC = 1.0$ g/m^3

c) 240s of ice accretion with $LWC = 1.5$ g/m^3

d) 180s of ice accretion with $LWC = 2.0$ g/m^3

Fig. 7 Measured 3D shapes of the ice structures accreted over the surface of the Pitot probe model under the icing conditions of $V_\infty = 40$ m/s and $T_\infty = -5°C$.

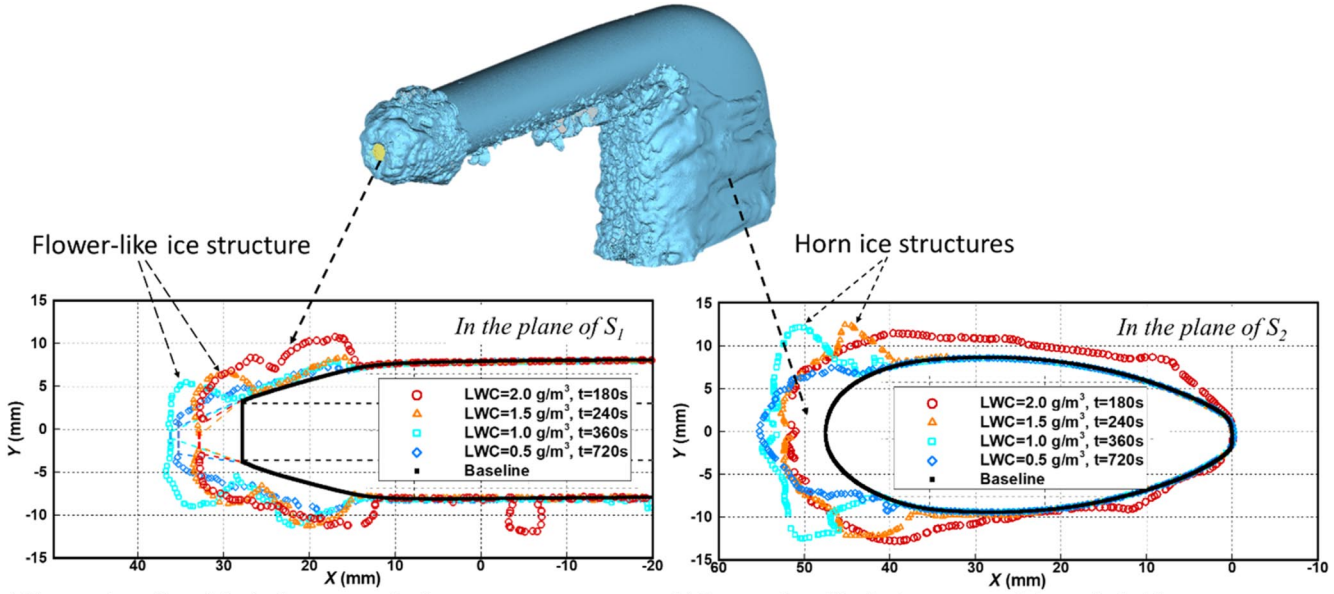

a) Extracted profiles of the ice layers near the front port

b) Extracted profiles ice layers around the probe holder

Fig. 8 Comparison of the extracted profiles of the ice layers accreted over the surface of the Pitot probe model under different test conditions.

given in Fig. 8 reveal quantitatively that the accreted ice layers for this case conformed well with the outer shape of the probe surface in general. No traces of water runback or ice accretion were observed over the back surface of the probe model. The 3D scanning measurement results confirm quantitatively that a rime icing process was taken place over the probe surface for this test case.

For the test case shown in Fig. 7b with the LWC of the incoming airflow being increased to $LWC = 1.0$ g/m^3, due to the insufficient convective and conductive heat transfer to dissipate all the released latent heat of fusion rapidly, a small portion of the impacted water mass would stay in the liquid phase over the ice accreting surface. While the accreted ice structures were found to become semi-opaque with a grainy appearance in general, the partially freezing nature of the mixed icing process was found to cause the formation of much more complicated ice shapes over the probe surface. While a flower-like ice structure was found to grow from the lip of the front port of the probe model, horn ice structures were also found to accrete over the front surface of the probe holder, as revealed quantitatively in Figs. 7b and 8b. The flower-like and horn ice structures were found to extrude further inside the incoming airflow to capture more airborne supercooled water droplets, which would further accelerate the growth of the irregular-shaped ice structures over the probe surface.

For the test case shown in Fig. 7c, as the LWC level of the incoming airflow was further increased to $LWC = 1.5$ g/m^3, more obvious runback of the unfrozen water was observed over the surface of the probe model. While the accreted ice structures were found to become almost transparent with a distinct glazy appearance, several rivulet-shaped runback ice structures were observed to accrete over the back surface of the probe holder. The extracted profiles of the accreted ice layers given in Fig. 8 also reveal clearly that, due to the existence of the substantial water runback flow over the ice accreting surface, the flower-like ice structure growing from the lip of the front port and the horn structures accreted over the frontal surface of the probe holder were found to become less distinguishable with their accretion sites moving to further downstream locations, in comparison to those of the test case of $LWC = 1.5$ g/m^3. The coverages of the ice layers accreted over the probe surface were found to become much greater, corresponding to the more dominant features of the glaze ice accretion for this mixed icing process.

As revealed clearly in Fig. 7d with $LWC = 2.0$ g/m^3, the ice accretion process over the surface of the probe model was found to become a typical glaze icing process, featured by the formation of transparent, glazy ice structures. Due to the significant water runback flowing over the ice accreting surface for this test case, the coverage of the ice layers accreted over the probe surface was found to be increased greatly. As revealed quantitatively from the extracted profiles of the ice layers given in Fig. 8, while the flower-like ice structure growing from the lip of the probe front port was found to become almost indistinguishable, no distinct horn structures were observed over the surface of the probe holder. The very "wet" nature of the glaze icing process caused the accreted ice layers to cover almost the entire surface of the probe holder, resulting in the blockage of the drain hole located at the back of the probe holder.

Based on the 3D scanning results shown in Fig. 7, the total volume of the accreted ice layers and, thereby, the total ice mass accreted on the probe model can also be determined for the test cases with different LWC values. According to Liu et al. [25], while the density of glaze ice is about 900 kg/m^3, the corresponding value is 880 kg/m^3 for typical rime ice. Hence, the total mass of the ice structures accumulated on the Pitot tube surface can also be estimated quantitatively. Because the mixed ice has the characteristics of both the glaze and rime ice, its density is estimated to be 890 kg/m^3. Figure 9 presents the measured total ice mass accreted on the probe model as a function of the LWC level of the incoming airflow. It can be seen clearly that, with the same Pitot probe model being exposed to almost the same amount of the airborne supercooled water droplets at $T_\infty = -5$°C, the total amount of the ice mass accreted over the surface of the Pitot probe model was found to increase almost exponentially with the LWC level of the incoming airflow. This is believed to be closely related to the changes in the ice accretion process under different test conditions.

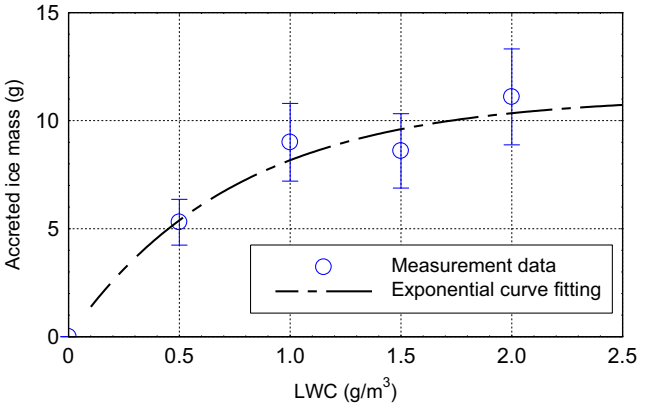

Fig. 9 The variations of the measured ice mass accreted on the Pitot probe model as a function of the LWC level of the incoming airflow at $T_\infty = -5.0$°C.

As described above, for the test case with $LWC = 0.5$ g/m^3, the ice accretion process under such a dry condition was a rime icing process with the accreted ice layers conforming well with the original profile of the probe model, resulting in relatively small projected area of the iced probe along the incoming airflow direction. As a result, only a small portion of the airborne water droplets would impact onto the probe surface, causing a relatively small amount of the accreted ice mass on the probe model.

As the LWC value of the incoming airflow increases, due to the insufficient convective and conductive heat transfer to dissipate all the released latent heat of fusion rapidly, unfrozen water was found to accumulate over the ice accreting surface, which would flow freely over the model surface as driven by the incoming airflow. As a result, the ice accretion over the probe surface was found to become a mixed icing or even a completely glaze icing process, depending on the LWC level of the incoming airflow. The partially freezing nature of the mixed or glaze icing process was found to cause the formation of much more irregular-shaped ice structures accreted over the model surface. While a flower-like ice structure was found to grow rapidly from the lip of the probe front port, horn ice structures were observed to form over the front surface of the probe holder. As shown clearly and quantitatively in Fig. 8, in comparison to the rime ice layer accreted over the probe surface, the irregular-shaped ice structures formed under the mixed or glaze icing conditions were found to extrude further into the incoming airflow, which would be able to capture more airborne water droplets over a much wider range to further accelerate the ice accretion process. Corresponding to the greater projected area of the iced probe model along the incoming flow direction, the total amount of the ice mass accreted on the probe model was found to increase exponentially with the increasing LWC level of the incoming airflow.

D. Characterizing the Ice Blockage to the Front Port Hole of the Pitot Probe Model Under Different Icing Conditions

As revealed clearly from the measurement results given above, the ice layers accreted along the lip of the front port of the Pitot probe model were found to become thicker and thicker as the ice accretion time increased, resulting in a continuously reduced size for the front port hole. The ice blockage to the front port could lead to misreadings of the airspeed from the iced Pitot probe, which can directly threat the aircraft inflight safety, leading to the loss of control over the aircraft.

A comprehensive image processing procedure as those described in Gao et al. [34] was used in the present study to process the acquired ice accretion images similar as those given in Figs. 2 and 3. The models used for the image processing include a Gaussian filtering operation for noise reduction and background removal, a binary treatment for edge enhancement, and a Canny method for edge identification. As a result, the variations of the front port hole size of the Pitot probe model were determined during the dynamic ice accretion processes. Figure 10 presents the image processing results to quantify the characteristics of the ice blockage to the probe front

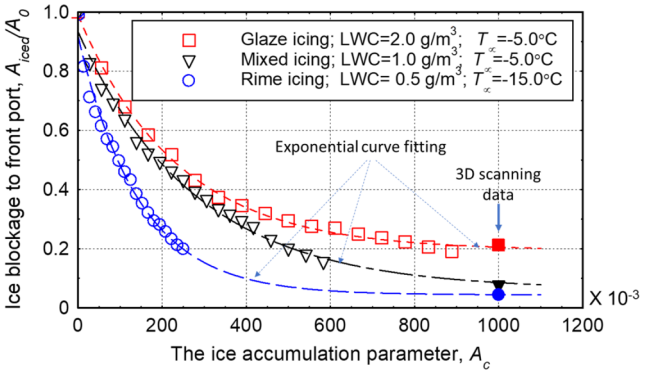

Fig. 10 Characterization of the ice blockage to the front port of the Pitot probe model under typical rime, mixed, and glaze icing conditions.

port as a function of the ice accretion time under the typical rime, mixed, and glaze icing conditions. In the plot, the ice blockage to the front port (i.e., A_{iced}/A_o) is defined as the ratio between the measured front hole area of the iced Pitot probe (i.e., A_{iced}) to its original value before starting the icing experiment (i.e., A_o). The ice accretion time was nondimensionalized as the corresponding value of the accumulation parameter of A_C by using Eq. (1). The measured ice blockage values based on the 3D profile scanning results of the iced Pitot probe model (i.e., at the ice accumulation parameter of $A_C \approx 1.0$) were also given in the plot for comparison.

As shown quantitatively in Fig. 10, the front hole size of the Pitot probe model was found to decrease monotonically with the increasing value of the ice accumulation parameter A_C, (i.e., the nondimensionalized ice accretion time). The relationship between the measured ice blockage ratio (i.e., A_{iced}/A_o) and the corresponding value of the ice accumulation parameter (i.e., A_C) were fitted very well with exponential functions for all the test cases. Interestingly, with the same value of the ice accumulation parameter of A_C, the ice blockage to the front port of the Pitot probe model was found to be the worst for the rime icing case, followed by the mixed icing, and then glaze icing scenarios. This can be explained by the facts that, with the Pitot probe exposed to almost the same amount of the airborne supercooled water droplets (i.e., as indicated by the same value of the ice accumulation parameter of A_C), because the supercooled water droplets would be frozen into ice instantly upon impacting onto the wedge-shaped lip of the probe's front port under the rime icing condition, the thickness of the ice layer accreted along the lip of the probe front port would increase rapidly, causing the significant ice blockage to the front port hole, as shown quantitatively in Fig. 4c. In comparison, because only a portion of the impacted supercooled water droplets would be frozen into ice immediately due to the insufficient heat transfer to dissipate the released latent heat of fusion under the glaze icing condition as described above, the rest of the impacted water mass would be transported rapidly to further downstream locations along the inner and outer walls of the front port hole. As a result, the thickness of the ice layer accreted along the lip of the probe front hole was found to become much smaller than that of the rime icing case, as shown quantitatively by the 3D scanning results given in Fig. 4, leading to the less ice blockage to the probe front hole. For the same reason, the ice layers accreted along the lip of the probe's front hole under the mixed icing condition would be thinner than the rime icing case, but thicker than the glaze icing case. Therefore, the ice blockage to the probe front hole for the mixed icing case was found to be in the middle among the three compared cases. As revealed clearly from the time-resolved measurements of the ice blockage data given in Fig. 10, within the limited icing experimental duration of the present study, the ice blockage ratio to the front port of the Pitot probe model was found to be more than 90% for the rime icing and the mixed icing cases. The front port of the Pitot probe model is expected to be blocked completely if the ice accretion parameter is further increased to enable more and more airborne supercooled water droplets impinging onto iced Pitot probe. It should also be noted that, even though the ice blockage to the front port of the Pitot probe model under the glaze icing condition was found to be less severe than the rime icing and mixed icing cases, the existence of the considerable water runback over the probe surface would cause the accreted glaze ice layers to cover almost entire probe surface. It would lead to the ice blockage to the static hole and even draining hole at the back of the probe holder, which would also cause misreadings of the airspeed from the iced Pitot probe and directly threaten the flight safety of the aircraft.

IV. Conclusions

In the present study, a comprehensive experimental investigation was conducted to examine the dynamic ice accretion process over the surfaces of an aeronautic Pitot probe for a better understanding of the underlying icing physics pertinent to Pitot probe icing phenomena. The experimental study was performed by leveraging the ISU-IRT with a typical aeronautic Pitot probe mounted inside the ISU-IRT for the icing experiments under different icing conditions (i.e., wet glaze, dry rime, and mixed icing conditions). During the icing experiments, while the airflow velocity was kept at $V_\infty = 40$ m/s for all the test cases, the ambient temperature was set at $T_\infty = -15°\text{C}$ for typical rime icing process. For the mixed and glaze icing experiments, while the ambient temperature was set to be $T_\infty = -5°\text{C}$, the LWC value of the incoming airflow was changed from $LWC \approx 0.50$ to 2.0 g/m^3. In addition to using a high-resolution imaging system to record the dynamic ice accretion process over the surface of the Pitot probe model, a DIP-based, 3D profile scanning system was utilized to quantify the 3D shapes of the ice layer accreted on the Pitot probe model. An ice accumulation parameter of A_C, which can be referred as the nondimensionalized ice accretion time with the effects of the LWC value being corrected, was used to characterize the experimental results obtained under different icing test conditions.

The characteristics of the ice accretion process over the surface of the Pitot probe model were found to depend strongly on the dynamic balance between two competing microphysical processes: 1) the continuous releasing of the latent heat of fusion associated with the solidification of the impacted supercooled water droplets over the model surface, and 2) the unsteady heat transfer process to dissipate the released latent heat of fusion from the ice accreting surface. For the rime icing test cases with colder ambient temperature and/or very low LWC level of the incoming airflow, the heat transfer process over the ice accreting surface (i.e., both heat convection via the frozen cold airflow and heat conduction through the metal substrate of the probe model) would be very intensive to dissipate/remove all the released latent heat of fusion rapidly. As a result, while ice accretion was found to be confined within narrow regions along the wedge-shaped lip of the probe front port and on the frontal surface of the probe holder, the accreted ice structures were found to be opaque and have milky-white appearance without any traces of water runback on the back surface of the probe model.

For the glaze and mixed icing cases with warmer ambient temperature and higher LWC level, while the heat transfer process became less intensive due to the warmer ambient temperature, more latent heat of fusion was released over the ice accreting surface corresponding to the larger amount of supercooled water droplets collected over the probe surface. As a result, only a portion of the impacted water droplets would be frozen into ice immediately, and the rest of the imparted water mass was found to stay in liquid phase until all the released latent heat of fusion was dissipated completely. Due to the complicated, dynamic interactions among the multiphase system (i.e., the unfrozen water flow over the probe surface, the solid ice accreted on the test model, and the frozen-cold incoming airflow), much more complicated, irregular-shaped ice structures were found to accreted over the probe surface (e.g., a flower-like ice structure growing rapidly from the lip of the front port and ice horn structures accreted over the front surface of the probe holder) under the mixed and glaze icing conditions. In comparison to the grainy rime ice layers accreted over the probe surface, the irregular-shaped ice structures accreted under the mixed and glaze icing conditions could extrude further into the incoming airflow to capture more airborne water droplets, further accelerating the growth of ice layers accreted on

the probe surface. As the LWC value increases, while the accreted ice layer was found to have a much greater coverage over the probe surface, the projected area of the iced Pitot probe model along the incoming flow direction was also found to increase monotonically. As a result, with the Pitot probe model being exposed to almost the same amount of the airborne supercooled water droplets (e.g., having the same value of the ice accumulation parameter of A_C), the total ice mass accreted over the probe surface was found to increase exponentially with increasing LWC level of the incoming airflow.

It was also found that, upon the impingement of the same amount of the supercooled water droplets carried by the incoming airflow, the front port of the Pitot probe model would be more readily blocked by rime ice accretion, followed by the mixed icing, and then glaze icing scenarios. While the ice blockage to the front port under the glaze icing condition was found to be less rigorous, the significant water runback over the probe surface caused the much greater ice coverage over the probe surface, leading to the complete blockage to the static pressure hole and even drain hole located at the back of the probe holder, which may also cause misreadings of the airspeed from the iced Pitot probe to impose a direct threat to the flight safety of the aircraft.

It should be noted that the research work presented here is a fundamental icing physics study with the primary objective to elucidate the underlying physics for a better understanding of Pitot probe icing phenomena. The effects of the design/operation parameters of the Pitot probes used for a specific aircraft on the ice accretion process are beyond the scope of the present study. A comprehensive experimental study is planned to examine the effects of important design/operation parameters of Pitot probes (e.g., probe geometry, materials of the probes, and the working Mach numbers) on the dynamic ice accretion over the surfaces of Pitot probes, and the research findings will be reported in the future. It should also be noted that an electrical heating element was embedded inside the probe holder for the Pitot probe model used in the present study. A follow-up investigation will also be conducted to evaluate the effectiveness of the electrical heating for the Pitot probe icing mitigation and protection.

Acknowledgments

The research work is partially supported by Iowa Space Grant Consortium Base Program for Aircraft Icing Studies. The support of National Science Foundation under award numbers of CBET-1916380 and CBET-1935363 is also gratefully acknowledged. The authors want to thank Yang Liu, James Benson, and Andrew Jordan of Iowa State University for their help in operating Iowa State University Icing Research Tunnel Facility.

References

[1] Campbell, S. E., Broeren, A. P., and Bragg, M. B., "Sensitivity of Aircraft Performance to Icing Parameter Variations," *Journal of Aircraft*, Vol. 44, No. 5, 2007, pp. 1758–1760. https://doi.org/10.2514/1.32355

[2] Cao, Y., Tan, W., and Wu, Z., "Aircraft Icing: An Ongoing Threat to Aviation Safety," *Aerospace Science and Technology*, Vol. 75, 2018, pp. 353–385. https://doi.org/10.1016/j.ast.2017.12.028

[3] Wang, X., Naterete, G. F., and Bibeau, E., "Convective Heat Transfer from a NACA Airfoil at Varying Angles of Attack," *Journal of Thermophysics and Heat Transfer*, Vol. 22, No. 3, 2008, pp. 457–463. https://doi.org/10.2514/1.34405

[4] Henry, R. C., Guffond, D., Bouveret, A., and Gardette, G., "Heat Transfer Coefficient Measurement on ICED Airfoil in a Small Icing Wind Tunnel," *Journal of Thermophysics and Heat Transfer*, Vol. 14, No. 3, 2000, pp. 348–354. https://doi.org/10.2514/2.6551

[5] Gao, L., Liu, Y., Zhou, W., and Hu, H., "An Experimental Study on the Aerodynamic Performance Degradation of a Wind Turbine Blade Model Induced by Ice Accretion Process," *Renewable Energy*, Vol. 133, April 2019, pp. 663–675. https://doi.org/10.1016/J.RENENE.2018.10.032

[6] Caliskan, F., and Hajiyev, C., "A Review of In-Flight Detection and Identification of Aircraft Icing and Reconfigurable Control," *Progress in Aerospace Sciences*, Vol. 60, July 2013, pp. 12–34. https://doi.org/10.1016/j.paerosci.2012.11.001

[7] Tian, L., Li, L., Hu, H., and Hu, H., "Experimental Study of Dynamic Ice Accretion Process over Rotating Aeroengine Fan Blades," *Journal of Thermophysics and Heat Transfer*, Vol. 35, No. 3, 2022, pp. 1–12. https://doi.org/10.2514/1.T6667

[8] Rhudy, M. B., Fravolini, M. L., Porcacchia, M., and Napolitano, M. R., "Comparison of Wind Speed Models within a Pitot-Free Airspeed Estimation Algorithm Using Light Aviation Data," *Aerospace Science and Technology*, Vol. 86, March 2019, pp. 21–29. https://doi.org/10.1016/j.ast.2018.12.028

[9] Spelay, R. B., Adane, K. F., Sanders, R. S., Sumner, R. J., and Gillies, R. G., "The Effect of Low Reynolds Number Flows on Pitot Tube Measurements," *Flow Measurement and Instrumentation*, Vol. 45, Oct. 2015, pp. 247–254. https://doi.org/10.1016/j.flowmeasinst.2015.06.008

[10] Siddique, M. A., Han, N., and Hu, H., "Development of an Experimental Unmanned-Aerial-System (UAS) to Study the Effects of Adverse Weathers on Its Flight Performance," *AIAA Science and Technology Forum and Exposition, AIAA SciTech Forum 2022*, AIAA Paper 2022-1646, 2022. https://doi.org/10.2514/6.2022-1646

[11] Jäckel, R., Gutiérrez-Urueta, G., and Tapia, F., "A Review on Pitot Tube Icing in Aeronautics: Research- Design and Characterization—Future Trends," *Flow Measurement and Instrumentation*, Vol. 81, Oct. 2021, Paper 102033. https://doi.org/10.1016/J.FLOWMEASINST.2021.102033

[12] Carbonara, V. E., and Binnie, A. G., "Icing of Pitot Static Tubes," *Journal of the Aeronautical Sciences*, Vol. 5, No. 10, 1938, pp. 400–403. https://doi.org/10.2514/8.678

[13] Ozcer, I., Switchenko, D., Baruzzi, G., and Chen, J., "Multi-Shot Icing Simulations with Automatic Re-Meshing," SAE Technical Paper 2019-01-1956, June 2019. https://doi.org/10.4271/2019-01-1956

[14] Zhang, H., Zhao, R., and Wen, C. Y., "Performance Deterioration of Pitot Tubes Caused by In-Flight Ice Accretion: A Numerical Investigation," *International Journal of Aerospace Engineering*, Vol. 2021, July 2021, p. 18. https://doi.org/10.1155/2021/5599116

[15] De Souza, J. R. B., Lisboa, K. M, Allahyarzadeh, A. B., de Andrade, G. J. A., Loureiro, J. B. R., Naveira-Cotta, C. P., Silva Freire, A. P., Orlande, H. R. B., Silva, G. A. L., and Cotta, R. M., "Thermal Analysis of Anti-Icing Systems in Aeronautical Velocity Sensors and Structures," *Journal of the Brazilian Society of Mechanical Sciences and Engineering*, Vol. 38, No. 5, 2016, pp. 1489–1509. https://doi.org/10.1007/s40430-015-0449-7

[16] Jäckel, R., Gutiérrez Urueta, G. L., Tapia Rodríguez, F., and Monreal Jiménez, C., "Numerical and Experimental Characterisation of an Aeronautic Pitot Probe," *Aeronautical Journal*, Vol. 123, No. 1264, 2019, pp. 890–911. https://doi.org/10.1017/aer.2019.33

[17] Lv, X., Guan, J., Wang, S., Zhang, H., Xue, S., Tang, Q., and He, Y., "Pitot Tube-Based Icing Detection: Effect of Ice Blocking on Pressure," *International Journal of Aerospace Engineering*, Vol. 2020, Aug. 2020, p. 8. https://doi.org/10.1155/2020/1902053

[18] Rodrigues, J., Grey, S., Azarpeyvand, M., and Rendall, T. C. S., "Acoustic Reflectometry for Pitot-Tube Blockage Detection," *Journal of Aircraft*, Vol. 55, No. 1, 2018, pp. 325–338. https://doi.org/10.2514/1.C034453

[19] Jarvinen, P. O., "Detection of Pitot-Static Icing at High Altitudes," *51st AIAA Aerospace Sciences Meeting Including the New Horizons Forum and Aerospace Exposition*, AIAA Paper 2013-0655, Jan. 2013. https://doi.org/10.2514/6.2013-655

[20] Waldman, R. M., and Hu, H., "High-Speed Imaging to Quantify Transient Ice Accretion Process over an Airfoil," *Journal of Aircraft*, Vol. 53, No. 2, 2016, pp. 369–377. https://doi.org/10.2514/1.C033367

[21] Liu, Y., and Hu, H., "An Experimental Investigation on the Unsteady Heat Transfer Process over an Ice Accreting Airfoil Surface," *International Journal of Heat and Mass Transfer*, Vol. 122, July 2018, pp. 707–718. https://doi.org/10.1016/j.ijheatmasstransfer.2018.02.023

[22] Peng, Y., Veerakumar, R., Zhang, Z., Hu, H., Liu, Y., He, X., and Hu, H., "An Experimental Study on Mitigating Dynamic Ice Accretion Process on Bridge Cables with a Superhydrophobic Coating," *Experimental Thermal and Fluid Science*, Vol. 132, April 2022, Paper 110573. https://doi.org/10.1016/J.EXPTHERMFLUSCI.2021.110573

[23] Gao, L., Liu, Y., and Hu, H., "An Experimental Investigation of Dynamic Ice Accretion Process on a Wind Turbine Airfoil Model Considering Various Icing Conditions," *International Journal of Heat and Mass Transfer*, Vol. 133, April 2019, pp. 930–939. https://doi.org/10.1016/J.IJHEATMASSTRANSFER.2018.12.181

[24] Politovich, M. K., "Predicting Glaze or Rime Ice Growth on Airfoils," *Journal of Aircraft*, Vol. 37, No. 1, 2000, pp. 117–121. https://doi.org/10.2514/2.2570

[25] Liu, Y., Bond, L. J., and Hu, H., "Ultrasonic-Attenuation-Based Technique for Ice Characterization Pertinent to Aircraft Icing Phenomena," *AIAA Journal*, Vol. 55, No. 5, 2017, pp. 1–8. https://doi.org/10.2514/1.J055500

[26] Makkonen, L., and Oleskiw, M. M., "Small-Scale Experiments on Rime Icing," *Cold Regions Science and Technology*, Vol. 25, No. 3, 1997, pp. 173–182. https://doi.org/10.1016/S0165-232X(96)00010-9

[27] Mangini, D., Antonini, C., Marengo, M., and Amirfazli, A., "Runback Ice Formation Mechanism on Hydrophilic and Superhydrophobic Surfaces," *Cold Regions Science and Technology*, Vol. 109, Jan. 2015, pp. 53–60. https://doi.org/10.1016/j.coldregions.2014.09.012

[28] Hansman, R. J., and Kirby, M. S., "Comparison of Wet and Dry Growth in Artificial and Flight Icing Conditions," *Journal of Thermophysics and Heat Transfer*, Vol. 1, No. 3, 1987, pp. 215–221. https://doi.org/10.2514/3.30

[29] Anderson, D., "Acceptable Tolerances for Matching Icing Similarity Parameters in Scaling Applications," *39th Aerospace Sciences Meeting and Exhibit*, AIAA Paper 2001-832, 2001. https://doi.org/10.2514/6.2001-832

[30] Gao, L., Veerakumar, R., Liu, Y., and Hu, H., "Quantification of the 3D Shapes of the Ice Structures Accreted on a Wind Turbine Airfoil Model," *Journal of Visualization*, Vol. 22, No. 4, 2019, pp. 661–667. https://doi.org/10.1007/s12650-019-00567-4

[31] Peng, Y., Veerakumar, R., Liu, Y., He, X., and Hu, H., "An Experimental Study on Dynamic Ice Accretion and Its Effects on the Aerodynamic Characteristics of Stay Cables with and without Helical Fillets," *Journal of Wind Engineering and Industrial Aerodynamics*, Vol. 205, Oct. 2020, Paper 104326. https://doi.org/10.1016/j.jweia.2020.104326

[32] Zhang, K., Tian, W., and Hu, H., "An Experimental Investigation on the Surface Water Transport Process over an Airfoil by Using a Digital Image Projection Technique," *Experiments in Fluids*, Vol. 56, No. 9, 2015, p. 173. https://doi.org/10.1007/s00348-015-2046-z

[33] Veerakumar, R., Gao, L., Liu, Y., and Hu, H., "Dynamic Ice Accretion Process and Its Effects on the Aerodynamic Drag Characteristics of a Power Transmission Cable Model," *Cold Regions Science and Technology*, Vol. 169, Jan. 2020, Paper 102908. https://doi.org/10.1016/j.coldregions.2019.102908

[34] Gao, L., Tao, T., Liu, Y., and Hu, H., "A Field Study of Ice Accretion and Its Effects on the Power Production of Utility-Scale Wind Turbines," *Renewable Energy*, Vol. 167, April 2021, pp. 917–928. https://doi.org/10.1016/j.renene.2020.12.014